The GALAH Survey: non-LTE departure coefficients for large spectroscopic surveys[⋆]

A. M. Amarsi[1], K. Lind[2,3], Y. Osorio[4,5], T. Nordlander[6,7], M. Bergemann[3], H. Reggiani[8], E. X. Wang[6,7], S. Buder[6,7], M. Asplund[6,7], P. S. Barklem[1], GALAH builders/smg, and Others

[1] Theoretical Astrophysics, Department of Physics and Astronomy, Uppsala University, Box 516, SE-751 20 Uppsala, Sweden
    e-mail: anish.amarsi@physics.uu.se
[2] Department of Astronomy, Stockholm University, AlbaNova University Centre, SE-106 91 Stockholm, Sweden
[3] Max Planck Institute for Astronomy, Königstuhl 17, 69117 Heidelberg, Germany
[4] Instituto de Astrofísica de Canarias, E-38205 La Laguna, Tenerife, Spain
[5] Departamento de Astrofísica, Universidad de La Laguna (ULL), E-38206 La Laguna, Tenerife, Spain
[6] Research School of Astronomy and Astrophysics, Australian National University, Canberra, ACT 2611, Australia
[7] ARC Centre of Excellence for All Sky Astrophysics in 3 Dimensions (ASTRO 3D), Australia
[8] Department of Physics and Astronomy, Johns Hopkins University, 3400 N Charles St., Baltimore, MD 21218, USA

May 25, 2020

ABSTRACT

Massive sets of stellar spectroscopic observations are rapidly becoming available, which can be used to determine the chemical makeup and evolution of the Galaxy with unprecedented precision. One of the major challenges in this endeavour is in constructing sufficiently realistic models of stellar spectra, with which to reliably determine stellar abundances. At present large stellar surveys commonly use simplified models that assume the stellar atmospheres are approximately in local thermodynamic equilibrium (LTE). To test and ultimately relax this assumption, we have performed non-LTE calculations for 13 different elements (H, Li, C, N, O, Na, Mg, Al, Si, K, Ca, Mn, and Ba), across an extensive grid of 3756 1D MARCS model atmospheres that spans up to $3000 \leq T_{\text{eff}}/\text{K} \leq 8000$, $-0.5 \leq \log g/\text{cm s}^{-1} \leq 5.5$, and $-5 \leq [\text{Fe/H}] \leq 1$. We present the grids of departure coefficients that have been implemented into the GALAH DR3 analysis pipeline, to complement the extant non-LTE grid for iron. We also present a detailed line-by-line reanalysis of 50126 distinct stars from GALAH DR3 in both LTE and non-LTE. We found that taking departures from LTE into account reduces the dispersion in the [A/Fe] versus [Fe/H] plane by as much as 0.1 dex, and can remove spurious differences between the dwarfs and giants by as much as 0.2 dex. The resulting abundance slopes can thus be qualitatively different in non-LTE, with different implications on the chemical evolution of our Galaxy. The grids of departure coefficients are publicly available, and can be implemented into LTE pipelines to make the most of observational data sets from large spectroscopic surveys.

Key words. atomic processes — radiative transfer — line: formation — stars: abundances — stars: atmospheres — stars: late-type

1. Introduction

Stellar astronomy has entered a new era characterised by extremely large surveys of stars and their spectra. Massive studies of stellar parameters and elemental abundances, based on medium- or high-resolution spectra of around 10^5 stars, are close to completion or have recently finished, including RAVE (Steinmetz et al. 2020; $R \sim 7500$), Gaia-ESO (Randich et al. 2013; $R \sim 20000$), APOGEE (Ahumada et al. 2019; $R \sim 22500$), and LAMOST (Zhao et al. 2012; $R \sim 7500$ in the medium-resolution setting). The near future will see a jump in the number statistics: the planned WEAVE (Dalton et al. 2016) and 4MOST (de Jong et al. 2019) surveys in the northern and southern hemispheres respectively should obtain high-resolution spectra for around 10^7 stars, while the third data release of Gaia (Gaia Collaboration et al. 2018) will include medium-resolution spectra of around 10^8 stars (Recio-Blanco et al. 2016). The ongoing Galactic Archaeology with HERMES (GALAH) survey falls somewhere in between these two groups, with the goal to observe 10^6 stars at relatively high resolution $R \sim 28000$ (De Silva et al. 2015).

Theoretical stellar spectra are used by all of these surveys, in order to obtain the stellar parameters and the elemental abundances. They are either directly compared against observations (García Pérez et al. 2016); or, in data-driven approaches (Ness et al. 2015; Ting et al. 2019) they are employed either in the analysis of training sets (Buder et al. 2018), and in the construction of gradient spectra (Xiang et al. 2019).

The absolute accuracy of these surveys thus depends on the reliability of their theoretical stellar spectra. Modelling deficiencies are a potential source of systematic error in these large surveys, that is often neglected for practical reasons. This is particularly relevant in the determination of stellar chemical compositions, or elemental abundances. While extra constraints can be placed on effective temperatures T_{eff} and surface gravities $\log g$ via interferometry, photometry, astrometry, and asteroseismology (Silva Aguirre et al. 2012; Karovicova et al. 2018), elemental abundances are in contrast most directly probed through absorption and emission lines in the stellar spectrum. It follows that deficiencies in the theoretical spectra have a direct impact on the reliability of the elemental abundance determinations.

A potential pitfall in classical spectroscopic analyses is the assumption that the stellar atmospheric matter satisfies local

---

[⋆] Grids of departure coefficients are publicly available via Zenodo (link here), or by contacting the lead author directly.

thermodynamic equilibrium (LTE; Mihalas & Athay 1973). For a given absorbing species, this simplifying assumption allows one to describe the populations of the different energy levels using Saha-Boltzmann statistics, enabling an immediate, analytical solution for the populations n_i and n_j of the lower and upper levels i and j for any given spectral line $i \leftrightarrow j$.

In reality, in the stellar photosphere the radiation field is non-Planckian; consequently interactions between light and matter cause the latter to depart from LTE. A more general description of the level populations is given by the equations of statistical equilibrium (Rutten 2003):

$$n_i \sum_j \left[R_{ij} + C_{ij} \right] = \sum_j n_j \left[R_{ji} + C_{ji} \right] \qquad (1)$$

In words, the net rate out of a level i is set by the balance between all the outwards and inwards radiative R and collisional C transitions. In the stellar interior Eq. 1 is satisfied trivially by virtue of detailed balance for LTE populations n_i^*:

$$n_i^* R_{ij} \equiv n_j^* R_{ji} \qquad (2)$$
$$n_i^* C_{ij} \equiv n_j^* C_{ji} \qquad (3)$$

In the stellar photosphere, Eq. 2 no longer holds; nevertheless, since to a good approximation the particles have Maxwell-Boltzmann distributions (Hubeny & Mihalas 2014), Eq. 3 remains true for LTE populations n_i^*. Thus, the matter can only satisfy LTE, $n_i = n_i^*$, if the collisional rates dominate over the radiative rates; in general, this is not the case.

Solving for the statistical equilibrium is much more demanding than simply assuming LTE. Eq. 1 indicates that all radiative and collisional transitions can affect the absorber populations and thus the spectral line. As well as being a much larger system of equations to solve, Eq. 1 must be iterated with a solution for the radiation field (Rybicki & Hummer 1992), and convergence problems are often encountered. Moreover, the final result is only as reliable as the input atomic data, and non-LTE calculations are founded on great efforts to calculate large sets of data describing energy levels, and radiative and collisional transition probabilities (Barklem 2016a), and to merge the various different data sets consistently into what are referred to as model atoms. In contrast, when modelling a spectral line in LTE, the populations are fixed and one only needs to have the partition functions describing that particular chemical species and the parameters of that particular line.

One way to improve the accuracy of classical spectroscopic analyses without significantly increasing their cost, is to apply precomputed non-LTE solutions to them. A common approach is to use precomputed abundance corrections Δ_l for a given spectral line l[1]:

$$[A/H]_l^{\text{non-LTE}} = [A/H]_l^{\text{LTE}} + \Delta_l \qquad (4)$$

Vast grids of line-by-line abundance corrections for many different atomic species already exist in the literature (e.g. Bergemann et al. 2012; Lind et al. 2012; Korotin et al. 2015; Mashonkina et al. 2016; Osorio & Barklem 2016; Amarsi et al. 2019b), that can readily be adopted and applied by the stellar spectroscopy community

---

[1] The absolute abundance of element A is defined as $\log \epsilon_A \equiv \log_{10}(N_A/N_H) + 12$, where N_A and N_H are the number of nuclei of element A and of hydrogen. Abundance ratios with respect are defined as $[A/H] \equiv \log \epsilon_A - \log \epsilon_{A\odot}$ and $[A/Fe] \equiv [A/H] - [Fe/H]$.

The line-by-line abundance corrections approach (Eq. 4) can become prohibitively complicated when a large number of spectral lines need to be studied simultaneously. It is simpler to instead apply non-LTE corrections to the level populations, because the number of relevant levels that would need to be considered roughly scales as the square root of the corresponding number of relevant spectral lines. This can be accomplished using precomputed grids of non-LTE departure coefficients β_i, for a given energy level i:

$$\beta_i \equiv \frac{n_i}{n_i^*} \qquad (5)$$

This approach requires some extra initial effort, because LTE spectrum synthesis codes need to be modified to read and manipulate the grids of departure coefficients. Nevertheless, grids of departure coefficients are desirable for large spectroscopic surveys, which are typically based on full-spectrum analyses.

Here, we present publicly-available grids of departure coefficients for 13 different elements: H, Li, C, N, O, Na, Mg, Al, Si, K, Ca, Mn, and Ba. For many of these elements, this is the most extensive set of non-LTE calculations: they cover 3756 1D model atmospheres that span the HR diagram from M-dwarfs, up the main sequence past the turn-off, to the tip of the red giant branch, with $-5 \leq [Fe/H] \leq 1$. Moreover this is the first time that a consistently computed grids of departure coefficients for multiple elements have been released in the literature.

In Sect. 2 we describe the non-LTE radiative transfer calculations, and the implementation of the resulting grids of departure coefficients into the GALAH analysis pipeline. In Sect. 3 we present a line-by-line reanalysis of 55159 spectra corresponding to 50126 distinct FGK-type field stars from GALAH DR3, and in Sect. 4 use these results to discuss the impact of the departure coefficients in practice. In Sect. 5 we briefly discuss the implication of our non-LTE abundance analysis in the context of Galactic chemical evolution, and in Sect. 6 we summarise and make some concluding remarks about the outlook of quantitative non-LTE stellar spectroscopy.

## 2. Calculation of departure coefficients

2.1. Model atoms

We list the 13 elements considered in this work and give the sizes of the corresponding model atoms, in Table 1. Full details about the physics included in each of the models can be found in the original papers, references to which are also provided in Table 1. We only provide a very brief overview of the models here.

The model atoms adopted here were all constructed recently, the oldest one being that for sodium (Lind et al. 2011). Minor changes were made to some of the models compared to what were presented in the original papers, in order to reduce the computational cost. In particular, for carbon, nitrogen, magnesium, and calcium, all fine structure levels were collapsed. This has previously been verified for carbon (Amarsi et al. 2019a) and oxygen (Amarsi et al. 2018a) to have only a small impact on the predicted departures from LTE: typically at most around 0.01 dex in terms of abundances.

For completeness, the model atom for iron is also listed in Table 1. Iron is treated in non-LTE in GALAH DR2 (Buder et al. 2018) and DR3 (Buder et al. in prep.). However the departure coefficients originate from an older set of calculations described in Amarsi et al. (2016b). They are not presented and discussed in the present study.
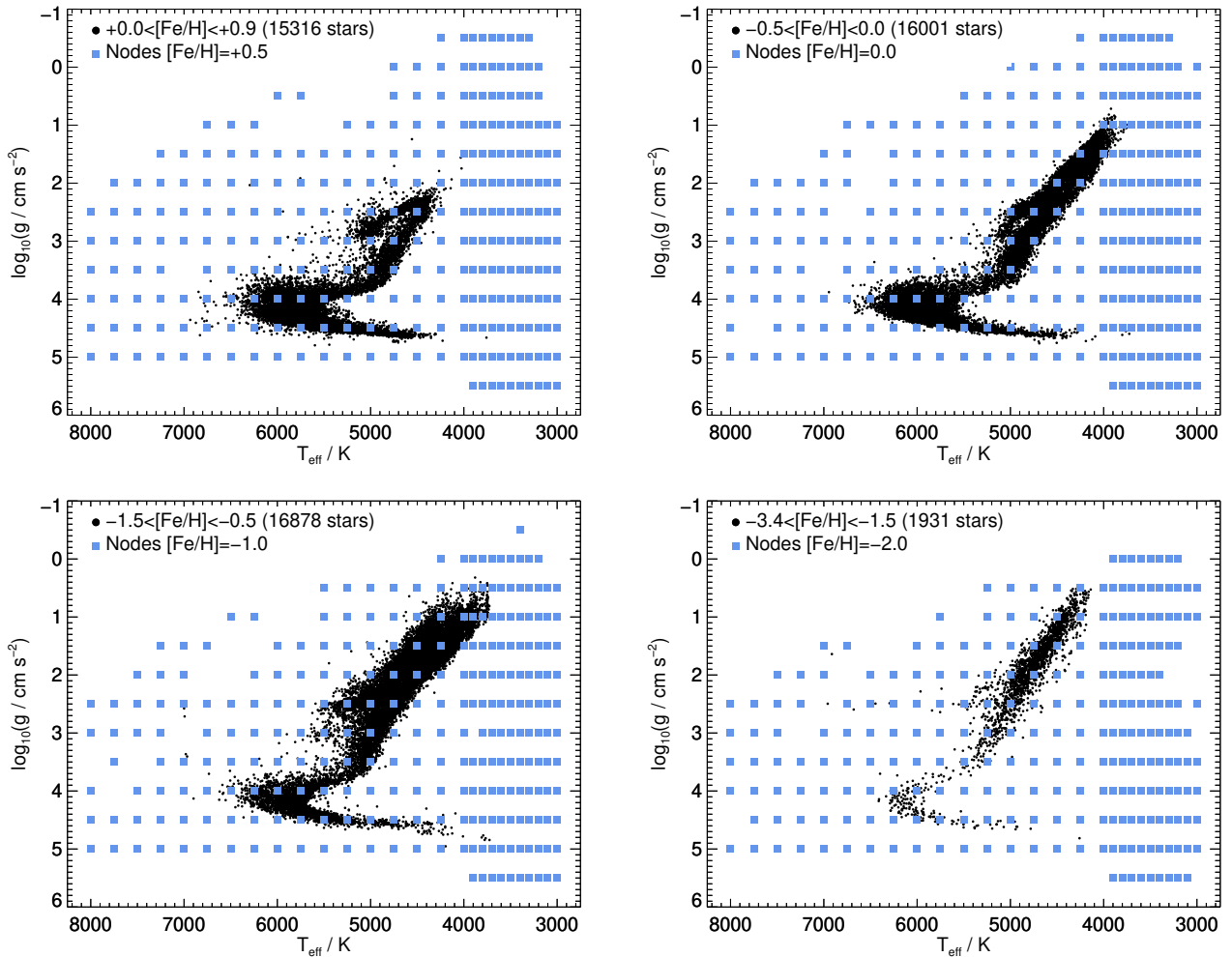
Fig. 1. Parameters of the 50126 stars drawn from GALAH DR3, studied in this work. Overplotted are the grid nodes at which the non-LTE radiative transfer calculations were carried out. The missing nodes are where standard MARCS model atmospheres do not presently exist, owing to convergence issues (see Sect. 5.4 of Gustafsson et al. 2008).
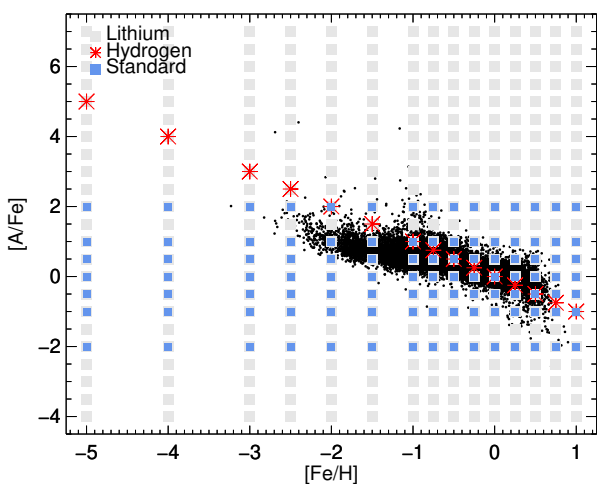
Fig. 2. Abundances and metallicities at which the non-LTE radiative transfer calculations were carried out. The calculations for hydrogen and lithium are specially noted. Also shown are the [O/Fe] for the sample of stars discussed in the present study.

Inelastic collisions with neutral hydrogen have historically been one of the largest sources of uncertainty in non-LTE models (Asplund 2005). Until recently, if such processes were not neglected completely, the classical Drawin recipe would usually be adopted. This recipe is based on the Thomson cross-section for ionisation by electron collisions (Thomson 1912), as modified for ionisation by atomic collisions by Drawin (1969, 1968), and later extended by Steenbock & Holweger (1984) and Lambert (1993) to also cover excitation. However, the Drawin recipe does not reflect the actual physics of the low-energy collisions occurring in stellar atmospheres (Barklem et al. 2011; Barklem 2016a; Belyaev & Yakovleva 2017). To attempt to correct for this, usually a single fudge factor S_H is calibrated and applied to the Drawin rate coefficients (Allende Prieto et al. 2004). This approach is not guaranteed to improve the reliability of the models: apart from introducing more free parameters into the spectroscopic analysis, this does not take into account that the errors in the Drawin recipe vary depending on the stellar parameters, and are transition-dependent. Moreover the Drawin recipe is unable to describe charge transfer processes ($A + H \leftrightarrow A^+ + H^-$), which are of astrophysical importance (Barklem et al. 2011).

All of the model atoms adopted here thus adopt physically-motivated descriptions for the inelastic collisions with neutral

Table 1. Elements considered here, and the number of levels, lines, and continua considered in the corresponding model atoms. The last column gives references for where the model atoms were originally presented. Iron is specially marked because the grids adopted in GALAH were already presented and discussed elsewhere in the literature.

Element	Species	# levels	# lines	# continua	Ref.
H	H I	20	190	20	1
	H II	1	-	-	
Li	Li I	20	113	20	2, 3
	Li II	1	-	-	
C	C I	46	343	45	4
	C II	1	-	-	
N	N I	31	174	32	5
	N II	2	-	-	
O	O I	47	322	47	6
	O II	3	-	-	
Na	Na I	22	166	22	7
	Na II	1	-	-	
Mg	Mg I	96	721	96	8
	Mg II	29	161	29	
	Mg III	1	-	-	
Al	Al I	42	135	33	9
	Al II	2	-	-	
Si	Si I	56	634	56	10
	Si II	1	-	-	
K	K I	133	250	133	11
	K II	1	-	-	
Ca	Ca I	67	937	67	12
	Ca II	24	89	24	
	Ca III	1	-	-	
Mn	Mn I	198	1645	198	13
	Mn II	82	44	-	
	Mn III	1	-	-	
Fe	**Fe I**	**421**	**3923**	**48**	**14, 15**
	Fe II	**41**	**77**	**-**	
	Fe III	**1**	**-**	**-**	
Ba	Ba I	8	-	8	16
	Ba II	102	284	102	
	Ba III	1	-	-	

References. (1) Amarsi et al. (2018b); (2) Lind et al. (2013); (3) Wang et al. (in prep.); (4) Amarsi et al. (2019a); (5) Amarsi et al. (2020); (6) Amarsi et al. (2018a); (7) Lind et al. (2011); (8) Osorio et al. (2015); (9) Nordlander & Lind (2017); (10) Amarsi & Asplund (2017); (11) Reggiani et al. (2019); (12) Osorio et al. (2019); (13) Bergemann et al. (2019); (14) Amarsi et al. (2016b); (15) Lind et al. (2017); (16) Gallagher et al. (2020).

hydrogen, instead of the Drawin recipe. For transitions involving low- and intermediate-lying levels of lithium (Belyaev & Barklem 2003; Barklem et al. 2003), sodium (Belyaev et al. 2010; Barklem et al. 2010), and magnesium (Belyaev et al. 2012; Barklem et al. 2012), cross-sections based on full quantum chemistry calculations were used. For the other species, asymptotic were used (Belyaev 2013; Barklem 2016b). Typically excitation of Rydberg levels were described using the free electron method (Kaulakys 1985, 1986, 1991).

2.2. Model atmospheres

The departure coefficients were calculated for a grid of 1D MARCS model atmospheres (Gustafsson et al. 2008), the same as is being used in the GALAH analysis pipeline (Buder et al. 2018; Buder et al. in prep.). The models are available from the online repository[2]; they specify the gas temperature, density, and other thermodynamic quantities, on 56 depth points. In this work, these quantities were not resampled and interpolated onto a new depth scale. This means that the departure coefficients presented here can readily be adopted and used consistently with the standard MARCS models.

We illustrate the extent of the grid of model atmospheres in Fig. 1 and Fig. 2. The 3756 different models are labelled by T_{eff}, $\log g$, and [Fe/H], and have the standard MARCS chemical compositions: namely, they adopt the solar chemical compositions of Grevesse et al. (2007), scaled with [Fe/H], and with an enhancement to α elements of +0.1, +0.2, +0.3, and +0.4 for [Fe/H] = −0.25, −0.5, −0.75, and [Fe/H] ≤ −1.0 respectively. Plane-parallel models with $\xi_{\mathrm{mic}} = 1.0\,\mathrm{km\,s^{-1}}$ were adopted for 'dwarfs' ($\log g \geq 4.0$), and spherically-symmetric models with $\xi_{\mathrm{mic}} = 2.0\,\mathrm{km\,s^{-1}}$ were adopted for 'giants' ($\log g \leq 3.5$).

2.3. Non-LTE radiative transfer

The departure coefficients were calculated using the MPI-parallelised non-LTE radiative transfer code Balder (Amarsi et al. 2018b), our modified version of Multi3D (Leenaarts & Carlsson 2009). The code takes as input a model atom (Sect. 2.1) and a model atmosphere (Sect. 2.2), which were discussed above. Balder uses the algorithm described in Sect. 2.4 of Rybicki & Hummer (1992) to solve the the equations of statistical equilibrium Eq. 1, together with the radiative transfer equation on short characteristics (Ibgui et al. 2013); the system of equations are closed by enforcing population conservation. Acceleration of convergence was achieved using the generalized conjugate residual algorithm (GCR; see the Appendix of Kao & Auer 1990, and Saad 2003).

The code Blue (Amarsi et al. 2016b) was used within Balder to determine the equation-of-state (assumed to be in LTE) and the background opacities (assumed to be in pure absorption, such that the background source function is equal to the Planck function). The bound-free (continuous) opacities were calculated on-the-fly, whereas the bound-bound (line) opacities were precomputed for different temperature-density-metallicity combinations, and interpolated at runtime. Care was taken not to double-count opacities already included in the model atoms. Partition functions and dissociation constants were drawn from Barklem & Collet (2016), and details of which background bound-bound and bound-free transitions were included can be found in Sect. 2.1.2 of Amarsi et al. 2016b.

The non-LTE radiative transfer calculations were performed independently for different elements, for a variety of elemental abundances, as we illustrate in Fig. 2. Generally, for a given element A, and for a given model atmosphere with chemical composition labelled by [Fe/H], calculations were performed for different abundances −2 ≤ [A/Fe] ≤ +2, keeping the abundances of all other elements fixed (employing the trace element approximation), but with the equation-of-state recomputed each time. There are some exceptions, however: for hydrogen, the calculations were kept strictly consistent with the composition of the

---

[2] marcs.astro.uu.se

model atmosphere; and for lithium, calculations were performed for $-4 \leq$ [Li/Fe] $\leq +7$.

The departure coefficients have a milder dependence on the input microturbulence parameter. A depth-independent microturbulence was adopted, the value of which was chosen to be consistent with that of the model atmosphere (Sect. 2.2): namely, $\xi_{\mathrm{mic}} = 1.0\,\mathrm{km\,s^{-1}}$ for dwarfs ($\log g \geq 4.0$), and $\xi_{\mathrm{mic}} = 2.0\,\mathrm{km\,s^{-1}}$ for giants ($\log g \leq 3.5$). Although the microturbulence is fixed to these values here for the calculation of the grid of departure coefficients, the microturbulence is varied in GALAH DR3 and in reanalysis we present in Sect. 3, as described in Buder et al. (2018).

The non-LTE calculations were assumed to have converged once the monochromatic emergent intensities changed by less than 0.01% between successive iterations. While the majority of the 383036 individual runs reached this convergence criterion, a small number (1858) of the runs did not. Various types of convergence problems affected the different runs, depending on the element and on the region of the parameter space. Given the scope of this project these problems could not be addressed individually. Nevertheless, we found that typically the departure coefficients of the uncoverged runs looked physically reasonable, after comparing against those from converged runs having similar stellar parameters. We include them in the data set, but cannot preclude the possibility of some unphysical behaviour in some regions of the parameter space.

2.4. Implementation of departure coefficients into LTE spectrum synthesis codes

The departure coefficients, defined by Eq. 5, are given for different energy levels i of the different elements A in Table 1, at each depth point z in the different model atmospheres labelled by T_{eff}, $\log g$, and [Fe/H] in Sect. 2.2:

$$\beta_i \equiv \beta_{i(\mathrm{A})}\,([\mathrm{A/Fe}], T_{\mathrm{eff}}, \log g, [\mathrm{Fe/H}], z) \qquad (6)$$

These data are publicly available via Zenodo (link here), or by contacting the lead author directly. They will also be distributed with SME and PySME (link here).

The grids of departure coefficients have been implemented into the GALAH analysis pipeline (Buder et al. 2018). They were used for determining the stellar parameters and elemental abundances in GALAH DR3 (Buder et al. in prep.). The pipeline uses the spectrum synthesis code Spectroscopy Made Easy (SME; Valenti & Piskunov 1996). Given a line list, SME looks for the departure coefficients of the lower and upper levels of all spectral lines by matching the total angular momentum quantum numbers J, electron configurations, and spectroscopic terms, specified in the grids. More details can be found in Sect. 3 of Piskunov & Valenti (2017).

3. Reanalysis of GALAH DR3 stars

3.1. Stellar sample

The full GALAH DR3 stellar sample (Buder et al. in prep.) includes 652799 spectra corresponding to 567115 distinct stars. The GALAH DR3 data products include T_{eff}, $\log g$, a first estimate of the iron abundance [Fe/H]$_{\mathrm{atmo}}$, microturbulence ξ_{mic}, and a broadening parameter v_{broad} that reflects the combined effects of stellar rotation and macroturbulence. These stellar parameters were determined simultaneously, with hydrogen modelled in non-LTE using the departure coefficients presented in

this work, and iron modelled in non-LTE using the departure coefficients presented in an older, but similar, set of calculations (Amarsi et al. 2016b). Also provided are elemental abundances [A/H], that were determined in a second step with the stellar parameters fixed. In particular, the non-LTE abundances were determined using the departure coefficients presented in this work. This includes a redetermination of the non-LTE iron abundance [Fe/H], that may differ from [Fe/H]$_{\mathrm{atmo}}$ that was determined in the first step.

To show the impact of the departure coefficients, a reanalysis of GALAH DR3 was carried out on 55159 spectra corresponding to 50126 distinct stars., selected from GALAH DR3 to be FGK-type field stars with reliable stellar parameters. The stellar parameters were fixed to the values provided with GALAH DR3, however the abundances were obtained using reduced GALAH spectra (Kos et al. 2017), in a line-by-line manner with the GALAH analysis pipeline (Buder et al. 2018). This reanalysis was necessary because LTE abundances are not provided with GALAH DR3, for the elements listed in Table 1. Moreover, GALAH DR3 does not include information about the line-by-line abundance dispersion, because these elemental abundances were determined from from simultaneous fits of all of the available lines of that element.

3.2. Line list and solar abundances

In Table 2 we list the lines used in the reanalysis of GALAH DR3. All of the elements in Table 1 were considered, except nitrogen, due to the lack of suitable lines within the GALAH spectral range. The line list has a large overlap with that of GALAH DR3 (Buder et al. in prep.).

We also list the adopted line-by-line absolute solar elemental abundances $\log \epsilon$ in Table 2. These were determined from the mean result from the solar twins in the sample: stars with T_{eff} within 100 K, $\log g$ within 0.1 dex, and [Fe/H] within 0.1 dex from the Sun (Nissen & Gustafsson 2018). For lithium the standard value of $\log \epsilon_{\mathrm{Li}} = 1.05$ (Asplund et al. 2009) is listed in Table 2, however the stellar lithium abundances discussed in this paper are given in the absolute sense, as per convention.

Subsequent sections are based on the abundance ratios [A/H] or [A/Fe] relative to the Sun; these were determined differentially on a line-by-line basis using the solar elemental abundances given in Table 2, prior to averaging over the lines. Thus, the absolute zero point in the results does not strictly reflect the solar standard, because there are small intrinsic dispersions in the elemental abundances of solar twins of the order 0.05 dex (Nissen 2015; Spina et al. 2016; Bedell et al. 2018), and because the lines employed by GALAH are different to the ones used when studying the solar chemical composition (Asplund et al. 2005). However, this method of normalising the elemental abundances is precise and puts the different spectral lines onto the same scale; it thus leads to a significant cancellation of errors originating from the adopted oscillator strengths, systematic offsets in the continuum placements, and the neglected effects of stellar surface convection. In the LTE results, this also cancels some of the errors arising from the neglected non-LTE effects, as we show in Sect. 4.1.

3.3. Stellar elemental abundances

We show the resulting elemental abundances for the entire sample of up to 50126 distinct stars in Figs 3 to 13. In Fig. 3 we show the absolute lithium abundances, $\log \epsilon_{\mathrm{Li}}$, as a function of [Fe/H],

Table 2. Lines used in the reanalysis of GALAH DR3 stars. The two components of the Li ɪ doublet were fit simultaneously. Also shown are the solar abundances inferred via the solar twins in the sample; the value for the Li ɪ doublet in brackets was adopted from the literature (Sect. 3.2). The final columns show the typical absolute abundance corrections ($\log \epsilon^{\text{non-LTE}} - \log \epsilon^{\text{LTE}}$) for each line: median results are shown in ($T_{\text{eff}}/K \pm 250$, $\log g/\text{cm s}^{-1} \pm 0.5$) regions corresponding to spectral/luminosity classes K V (5000, 4.5), F V (6500, 4.0), and K III (4250, 2.0); the most severe corrections for a given line are highlighted, and no results are shown for where the lines were too weak to be detected.

Spec.	λ_{air}/nm	χ_{low}/eV	$\log gf$	Ref.	$\log \epsilon_\odot^{\text{NLTE}}$	$\log \epsilon_\odot^{\text{LTE}}$	0 < [Fe/H] < 1			−2 < [Fe/H] < −1		
							K V	F V	K III	K V	F V	K III
Li ɪ	670.776	0.000	−0.002	1	(1.05)	(1.05)	−0.02	−0.07	+0.02	−0.05	**−0.10**	−0.02
	670.791	0.000	−0.303									
C ɪ	658.761	8.537	−1.021	2	8.43	8.43	+0.00	−0.01	+0.00		**−0.03**	+0.00
O ɪ	777.194	9.146	+0.369	3	8.79	8.99	−0.08	**−0.52**	−0.12	−0.06	−0.16	−0.12
O ɪ	777.417	9.146	+0.223	3	8.80	8.98	−0.07	**−0.48**	−0.13	−0.04	−0.15	−0.12
O ɪ	777.539	9.146	+0.002	3	8.79	8.94	−0.08	**−0.42**	−0.07	−0.05	−0.13	−0.12
Na ɪ	568.263	2.102	−0.706	4	6.04	6.19	−0.13	−0.17	**−0.23**	−0.10	−0.11	−0.12
Na ɪ	568.821	2.104	−0.404	4	6.05	6.24	−0.14	**−0.23**	−0.19	−0.10	−0.11	−0.17
Mg ɪ	571.109	4.346	−1.724	5	7.59	7.63	−0.06	−0.05	**−0.18**	−0.03	+0.02	−0.11
Al ɪ	669.867	3.143	−1.870	6	6.39	6.41	−0.03	−0.01	**−0.10**	−0.03		−0.09
Al ɪ	783.531	4.022	−0.689	6	6.41	6.43	−0.03	−0.02	**−0.13**	−0.03	+0.00	−0.07
Si ɪ	568.448	4.954	−1.553	7, 8	7.39	7.42	−0.02	−0.03	**−0.08**	−0.01	−0.01	−0.06
Si ɪ	569.043	4.930	−1.773	7, 8	7.43	7.44	−0.01	−0.02	**−0.06**	−0.01	−0.01	−0.05
Si ɪ	570.110	4.930	−1.953	7, 8	7.49	7.50	−0.01	−0.02	−0.03	−0.01	−0.01	**−0.04**
Si ɪ	577.215	5.082	−1.653	7, 8	7.50	7.52	−0.01	−0.02	**−0.07**	−0.01	−0.01	−0.04
Si ɪ	579.307	4.930	−1.963	7, 8	7.48	7.50	−0.01	−0.02	**−0.11**	−0.01	−0.01	−0.04
Si ɪ	768.027	5.863	−0.590	7, 8	7.57	7.61	−0.04	−0.06	**−0.25**	−0.02	−0.02	−0.11
K ɪ	769.896	0.000	−0.178	9	5.05	5.49	−0.21	−0.62	−0.30	−0.28	−0.34	**−0.66**
Ca ɪ	586.756	2.933	−1.570	10	6.32	6.32	−0.01	−0.01	**−0.03**	−0.01	+0.03	−0.01
Ca ɪ	649.965	2.523	−0.818	11	6.27	6.31	−0.05	+0.01	+0.02	**−0.06**	+0.01	−0.01
Mn ɪ	475.404	2.282	−0.080	12	5.29	5.28	+0.00	+0.00	+0.02	+0.06	**+0.14**	+0.10
Mn ɪ	476.151	2.953	−0.274	12	5.36	5.34	+0.01	+0.03	+0.02	+0.05	+0.10	**+0.12**
Ba ɪɪ	585.367	0.604	−0.907	13	2.13	2.22	−0.04	**−0.14**	−0.03	−0.01	−0.01	−0.12
Ba ɪɪ	649.689	0.604	−0.407	13	2.23	2.42	−0.10	**−0.29**	−0.07	−0.07	−0.11	−0.18

References. (1) Yan et al. (1998); (2) Hibbert et al. (1993); (3) Hibbert et al. (1991); (4) Froese Fischer et al. (2006); (5) Chang & Tang (1990); (6) Kelleher & Podobedova (2008); (7) Garz (1973); (8) O'Brian & Lawler (1991); (9) Trubko et al. (2017); (10) Smith (1988); (11) Smith & Raggett (1981); (12) Den Hartog et al. (2011); (13) Davidson et al. (1992).

and in the other figures we show the run of [A/Fe] for the different elements considered in this study, from carbon to barium. For each element the non-LTE and LTE results are shown in separate panels; the non-LTE iron abundance was adopted from GALAH DR3 in all cases. The plots only include those stars for which both LTE and non-LTE abundances were obtained; therefore, the same number of stars are included in the left and right panels of each figure. The results were also binned, separately for dwarfs ($\log g > 3.5$) and for giants ($\log g < 3.5$), and these are overplotted to illustrate the average abundance trends.

There are several features in Figs 3 to 13 that best illustrate the impact of taking departures from LTE into account, that we discuss in turn below: the typical non-LTE abundance corrections (Sect. 4.1), the appearance of the average abundance trends (Sect. 4.2), the differences between the results for dwarfs and giants (Sect. 4.3), and the overall dispersions in the elemental abundances (Sect. 4.4).

4. Discussion

4.1. Typical non-LTE abundance corrections

In Table 2 we show the typical line-by-line differences between the absolute abundances inferred in non-LTE and in LTE: $\log \epsilon_A^{\text{non-LTE}} - \log \epsilon_A^{\text{LTE}}$. These are based on the abundances in-

ferred from the present sample, and are shown for the extreme edges of the HR diagram illustrated in Fig. 1 and the abundance plane illustrated in Fig. 2, that is for K dwarfs, F dwarfs, and K giants, at high and low metallicities.

In metal-rich F dwarfs, the absolute abundance corrections can be as severe as −0.6 dex for the K ɪ 769.9 nm resonance line (Reggiani et al. 2019), −0.5 dex for the O ɪ 777 nm triplet (Amarsi et al. 2016a), and −0.3 dex for the Ba ɪɪ 649.7 nm line (Korotin et al. 2011; Gallagher et al. 2020). Typically the most severe absolute abundance corrections are found for metal-rich K-giants; it is also in this cooler, lower-pressure regime where inelastic hydrogen collisions (Sect. 2.1) play a greater role.

Table 2 shows that for a particular species, the absolute abundance correction goes in the same direction and is of a similar magnitude for the different lines of the given species: the non-LTE effects are of a similar nature for the lines of a given species. A consequence of this is that in the present analysis, non-LTE effects do not average out simply by using multiple lines of the same species. It is beyond the scope of this paper to discuss the non-LTE effects for each of the spectral lines and elements considered here, and instead refer the reader to the papers listed in Table 1 for further details.

It is important to note that with the exception of lithium (Fig. 3), the abundance results presented in Sect. 3.3 are differential in the sense that the LTE and non-LTE solar abundances pre-

Table 3. Relative abundance corrections ($[A/H]^{\text{non-LTE}} - [A/H]^{\text{LTE}}$) for each element. Line-by-line solar abundances in non-LTE and in LTE were adopted to determine line-by-line $[A/H]_l^{\text{non-LTE}}$ and $[A/H]_l^{\text{LTE}}$ respectively, from which mean values were adopted. Median results are shown in ($T_{\text{eff}}/K \pm 250$, $\log g/\text{cm s}^{-1} \pm 0.5$) regions corresponding to spectral/luminosity classes K V (5000, 4.5), F V (6500, 4.0), and K III (4250,2.0); the most severe corrections for a given element are highlighted, and no results are shown for where all the diagnostic lines were too weak to be detected.

Element	0 < [Fe/H] < 1			−2 < [Fe/H] < −1		
	K V	F V	K III	K V	F V	K III
Li	−0.02	−0.07	+0.02	−0.05	**−0.10**	−0.02
C	+0.00	−0.01	+0.01		**−0.02**	+0.00
O	+0.12	**−0.29**	+0.06	+0.14	+0.03	+0.06
Na	+0.03	−0.03	−0.04	**+0.07**	+0.07	+0.02
Mg	−0.01	−0.01	**−0.14**	+0.02	+0.06	−0.07
Al	−0.01	+0.01	**−0.09**	−0.01	+0.03	−0.06
Si	+0.01	+0.00	**−0.08**	+0.02	+0.02	−0.04
K	**+0.24**	−0.18	+0.15	+0.16	+0.10	−0.22
Ca	−0.02	+0.02	+0.01	−0.03	**+0.04**	+0.00
Mn	−0.01	+0.00	−0.01	+0.05	**+0.14**	+0.09
Ba	+0.07	−0.08	+0.09	**+0.11**	+0.08	−0.01
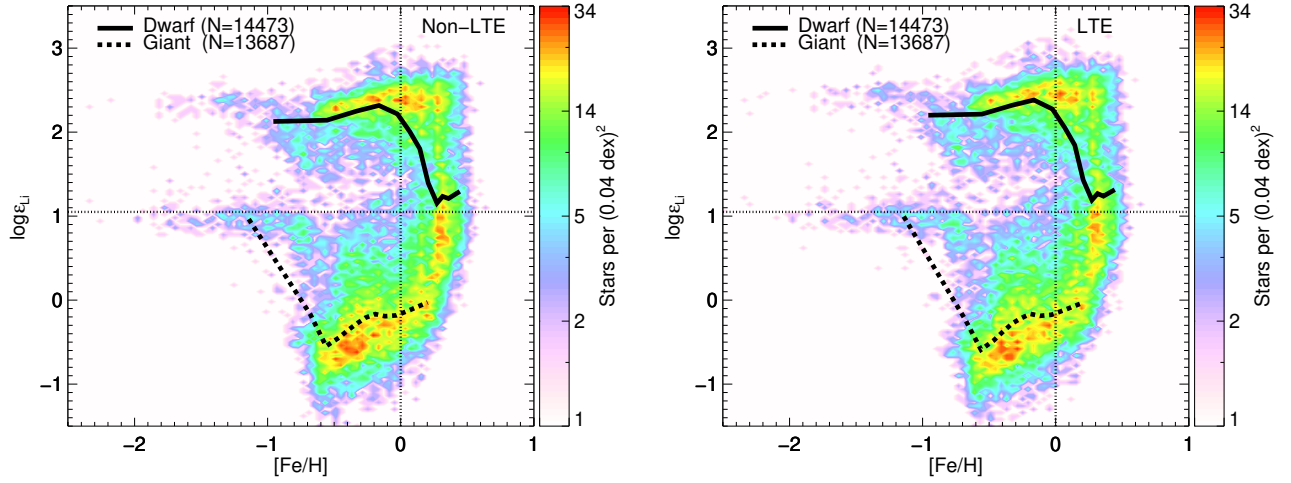
Fig. 3. Results for lithium. Left panel shows non-LTE results, right panel shows LTE results. Binned data for dwarfs ($\log g > 3.5$) and for giants ($\log g < 3.5$) are overplotted.
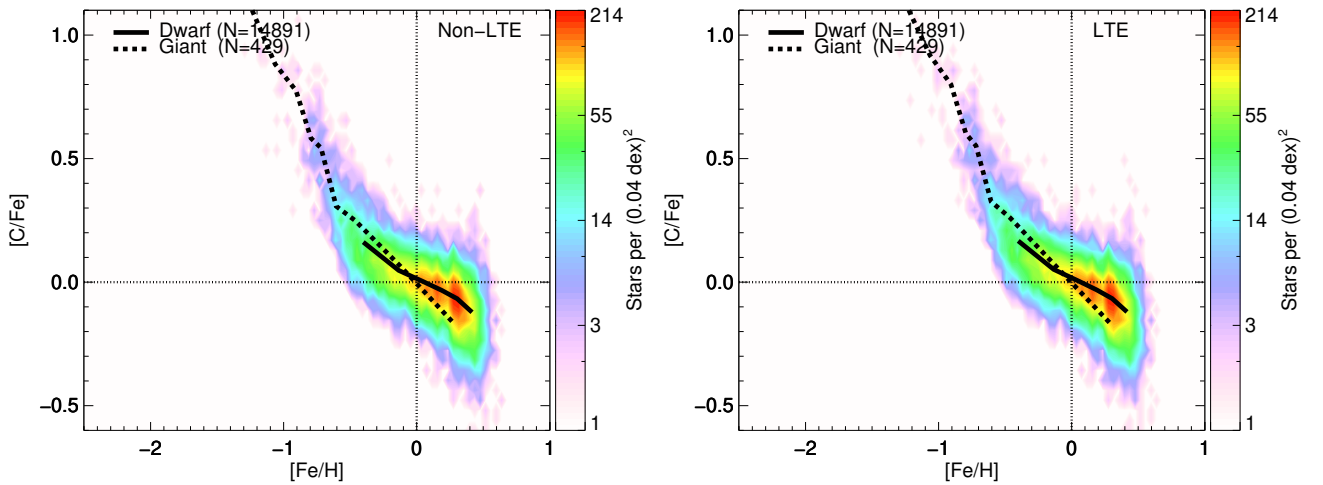
Fig. 4. Results for carbon. Left panel shows non-LTE results, right panel shows LTE results. Binned data for dwarfs ($\log g > 3.5$) and for giants ($\log g < 3.5$) are overplotted.
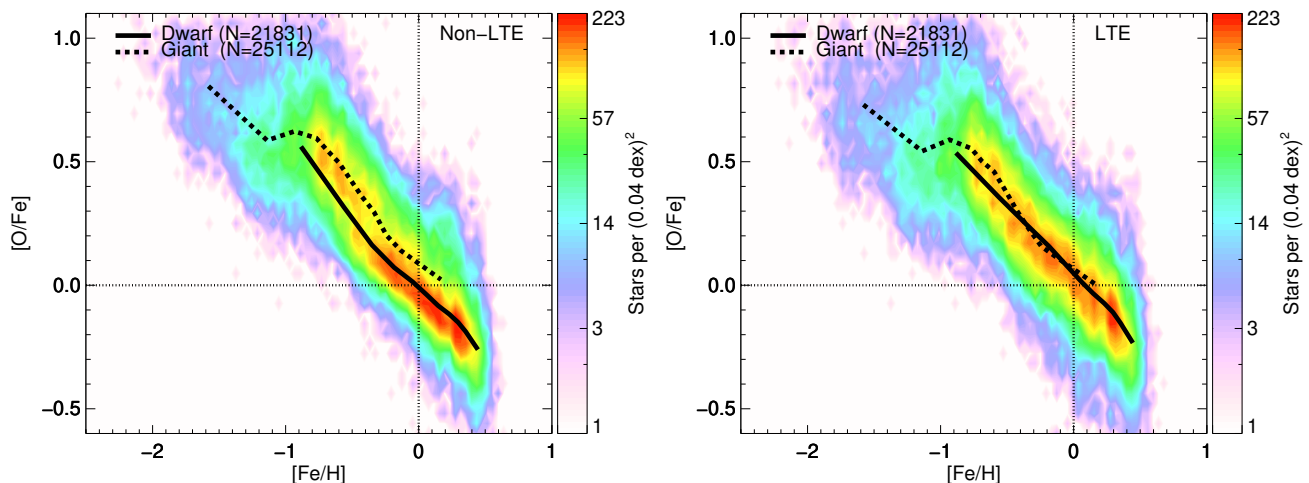
Fig. 5. Results for oxygen. Left panel shows non-LTE results, right panel shows LTE results. Binned data for dwarfs (log g > 3.5) and for giants (log g < 3.5) are overplotted.
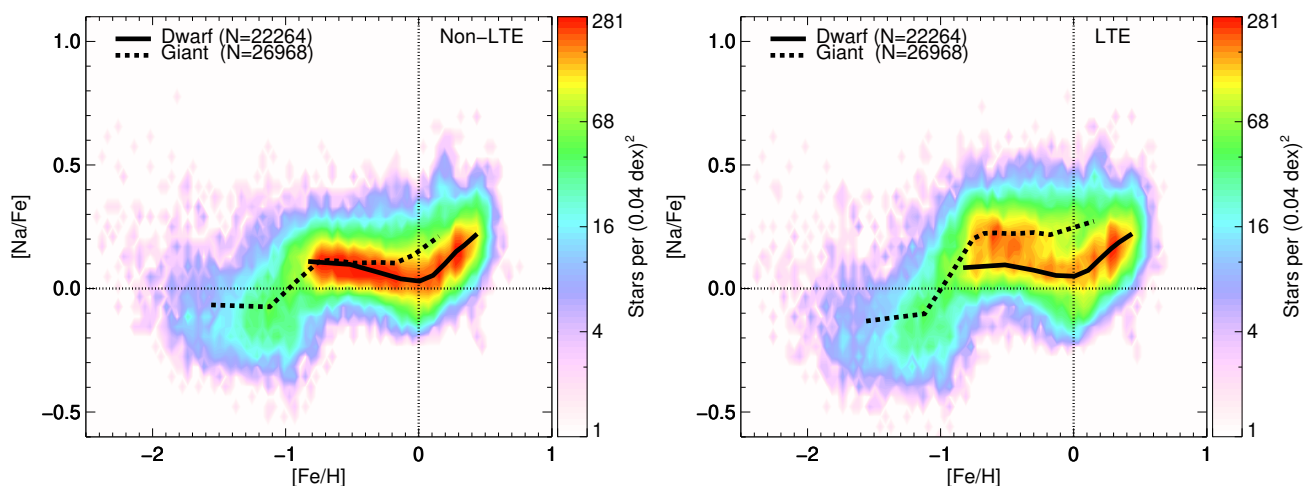
Fig. 6. Results for sodium. Left panel shows non-LTE results, right panel shows LTE results. Binned data for dwarfs (log g > 3.5) and for giants (log g < 3.5) are overplotted.

sented in Table 2 were used to convert absolute elemental abundances $\log \epsilon_{Al}$ into abundance ratios $[A/H]_l$ or $[A/Fe]_l$ relative to the Sun, for given lines l. These quantities were then averaged over the different lines l, to obtain the final abundance ratios $[A/H]$ or $[A/Fe]$. This results in a more accurate zero point, and, for the elements with multiple line diagnostics, lower dispersion, owing to significant cancellation of systematic errors as we discussed in Sect. 3.2.

Thus in Table 3 we show the typical relative abundance corrections $[A/H]^{\text{non-LTE}} - [A/H]^{\text{LTE}}$ for each element, determined line-by-line differentially prior to averaging, using the line-by-line solar abundances listed in Table 2. The severity of the differential non-LTE effects are less than of the absolute non-LTE effects as expected; for example, the differential corrections reach at most only −0.3 dex for the O I 777 nm triplet, whereas the absolute corrections are −0.5 dex (reflecting that the non-LTE correction in the Sun is roughly −0.2 dex). This cancellation is less effective for stars further away from the Sun in parameter space; for example in cooler stars, or in the metal-poor regime, pro-

vided that the absolute non-LTE effects are indeed severe, and that they are sensitive to the stellar parameters.

4.2. Non-LTE effects on abundance trends

We find that the assumption of LTE can lead to average abundance trends that are quantitatively and sometimes even qualitatively different compared to what is found in non-LTE. This is particularly apparent for a few elements: sodium, magnesium, potassium, and manganese, where there are differences in the mean $[A/Fe]$ at given $[Fe/H]$ of up to around 0.2 dex, resulting in qualitatively different pictures of the Galactic chemical evolution.

For sodium (Fig. 6), in LTE, there is a jump in $[Na/Fe]$ of from −0.2 dex to +0.2 dex as $[Fe/H]$ increases past −1.0 dex. In non-LTE, this jump of 0.4 dex is reduced to just 0.2 dex, with $[Na/Fe]$ increasing from −0.1 dex to +0.1 dex.

For magnesium (Fig. 7) in LTE there is a clear local maximum in $[Mg/Fe]$ of around 0.45 dex at $[Fe/H] \approx -0.75$. In
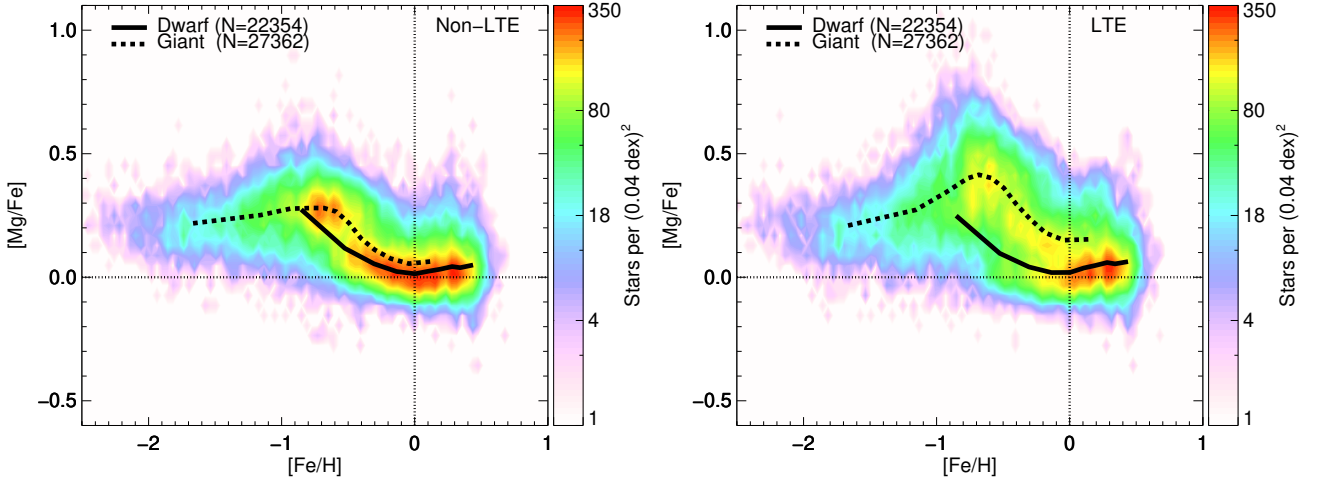
Fig. 7. Results for magnesium. Left panel shows non-LTE results, right panel shows LTE results. Binned data for dwarfs (log g > 3.5) and for giants (log g < 3.5) are overplotted.
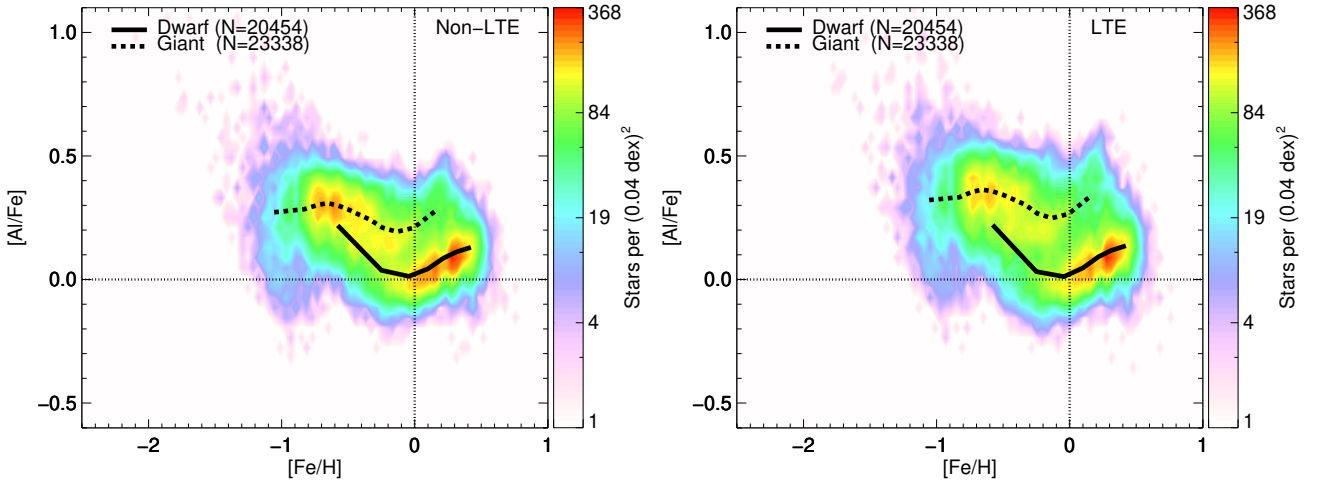
Fig. 8. Results for aluminium. Left panel shows non-LTE results, right panel shows LTE results. Binned data for dwarfs (log g > 3.5) and for giants (log g < 3.5) are overplotted.

non-LTE, [Mg/Fe] shows the usual plateau at low metallicties at around 0.25 dex, and a decreasing trend towards higher metallicities.

For potassium (Fig. 10), there is also a local maximum in LTE, with [K/Fe] peaking at around 0.45 dex at [Fe/H] ≈ −1.0. There is also a linear decrease in [K/Fe] at super-solar metallicities. In non-LTE, potassium instead shows a trend similar to the α-elements, plateauing at [K/Fe] ≈ 0.25 for [Fe/H] ≲ −1.0, and showing a flat trend at super-solar metallicities.

Finally for manganese (Fig. 12), in LTE, [Mn/Fe] increases rather steeply from −0.5 dex at [Fe/H] ≈ −2.0, up to 0.2 dex at [Fe/H] ≈ 0.5. In non-LTE instead, [Mn/Fe] plateaus at low metallicities at around −0.3 dex below [Fe/H] ≲ −1.0, and the abundance trend is less steep.

4.3. Non-LTE effects on offsets between dwarfs and giants

We find that the assumption of LTE can impart large offsets between dwarfs and giants in abundance space. That is, the gi-

ants tend to sit either far above or below the dwarfs in [A/Fe] versus [Fe/H] space, even if the abundance tracks are parallel to each other, This offset is as large as 0.3 dex in the case of magnesium (Fig. 7); smaller offsets can also be seen for sodium (Fig. 6), silicon (Fig. 9), and potassium (Fig. 10). These offsets shrink significantly for each of these elements when non-LTE methods are used. For example, for sodium it is reduced by around 0.2 dex, and the tracks are in good agreement between −1 ≲ [Fe/H] ≲ −0.5.

For some elements, taking non-LTE effects into account does not negate entirely the offsets between the dwarfs and giants. The residual offsets for most elements tend to be only of the order 0.05 dex. For aluminium (Fig. 8) and barium (Fig. 13), the offsets reach 0.2 dex. These large offsts may reflect other systematic errors within the GALAH analysis pipeline.

For the α-elements oxygen (Fig. 5), magnesium (Fig. 7), and silicon (Fig. 9), the residual offsets in non-LTE amount to around 0.1 dex. These offsets may in part be due to selection effects: the giants are brighter and observed to larger distances, and thus probe more of the α-rich Galactic thick disk; conversely, the
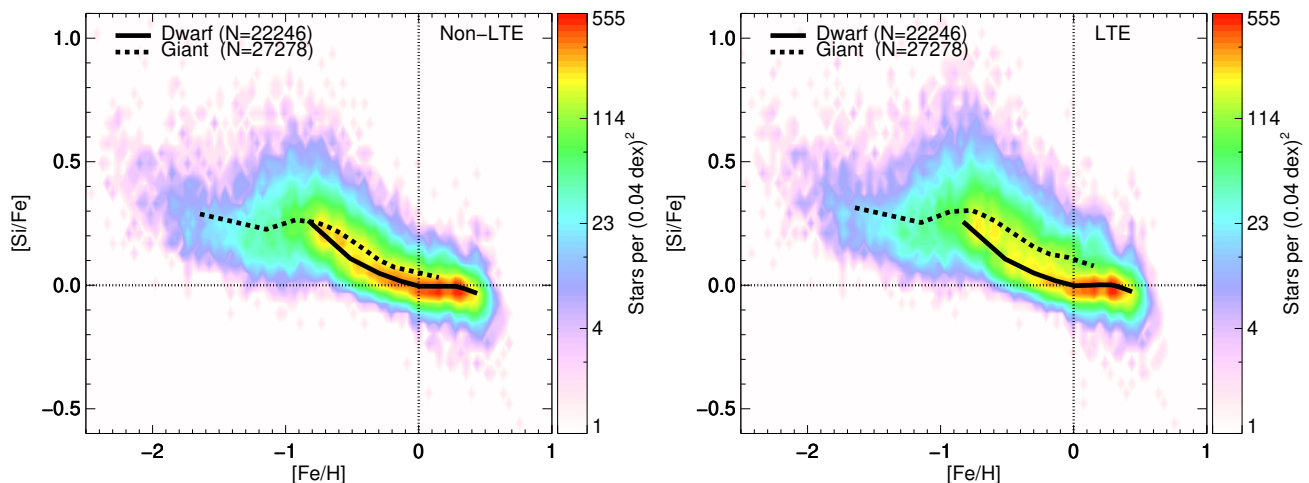
Fig. 9. Results for silicon. Left panel shows non-LTE results, right panel shows LTE results. Binned data for dwarfs ($\log g > 3.5$) and for giants ($\log g < 3.5$) are overplotted.
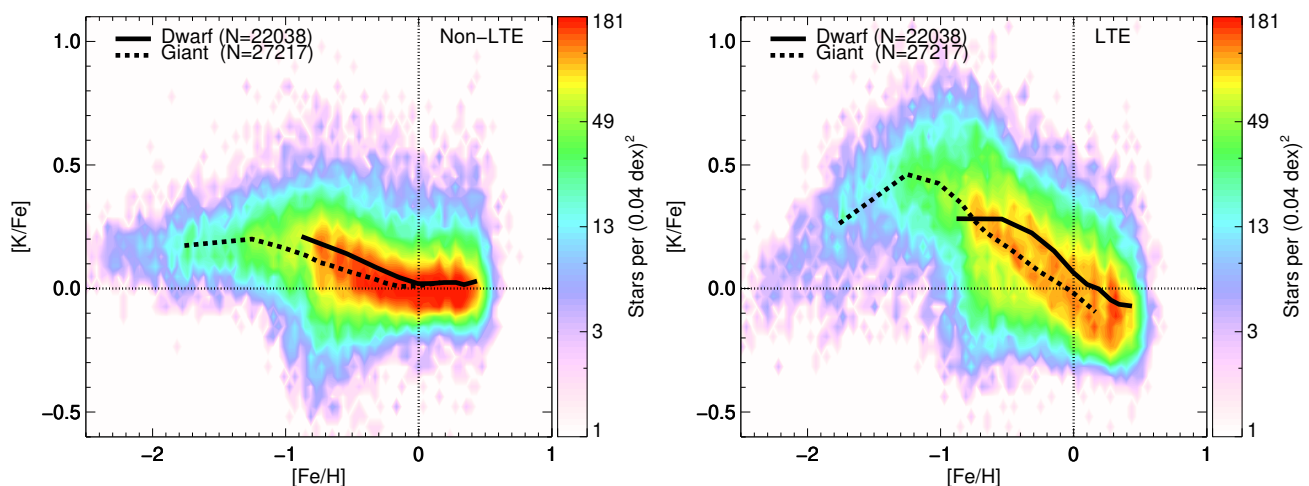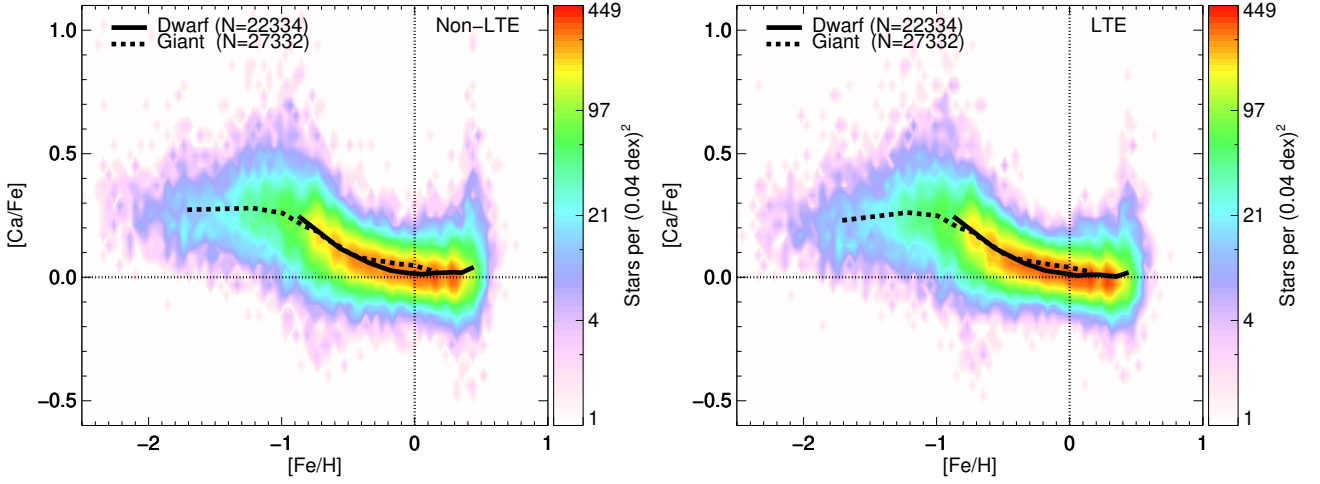

Fig. 10. Results for potassium. Left panel shows non-LTE results, right panel shows LTE results. Binned data for dwarfs ($\log g > 3.5$) and for giants ($\log g < 3.5$) are overplotted.

dwarfs probe more of the α-poor Galactic thin disk (Hayden et al. 2015; Feuillet et al. 2019). However, one would then expect a similar offset for calcium (Fig. 11), whereas instead the mean trends for the dwarfs and giants lie on top of each other. This may reflect residual systematics with the non-LTE calcium abundances. For instance, Osorio et al. (2020) showed recently that non-LTE Mg I continuous opacities can make a significant impact on the predicted Ca I departure coefficients; this effect is not taken into account in the present calculations.

4.4. Non-LTE effects on abundance dispersions

We find that the assumption of LTE can substantially increase the spread of [A/Fe] at given [Fe/H]. This is immediately evident by comparing the densities of stars in LTE and non-LTE in many of the plots presented in in Sect. 3.3, and is particularly obvious for oxygen (Fig. 5), sodium (Fig. 6), magnesium (Fig. 7), and potassium (Fig. 10).

The dispersions in the stellar elemental abundances can also be quantified. In Fig. 14 we show the median standard deviation in [A/Fe] (or for lithium, $\log \epsilon_{\mathrm{Li}}$) across the different bins shown in Figs 3 to 13, separately for dwarfs, and for giants; this is labelled 'Star-to-star'. For comparison, also plotted are the median standard deviations in [A/Fe] over multiple spectral lines, as inferred for a given element and for a given star (after already averaging over multiple observations, if necessary); this is labelled 'Line-to-line'. Another comparison can be made, by noting that there are 3237 stars in the sample of 50126 for which two or more observations exist. Thus, the median standard deviations in [A/Fe] over multiple observations of the same stars are also plotted; this is labelled 'Multiple obs.'.

The assumption of LTE does not significantly impact the dispersions in the results from multiple observations. This reflects the random noise arising from the GALAH analysis pipeline that are propagated from the finite signal-to-noise ratios of the observations into the inferred abundances, either directly or via the inferred stellar parameters. In Fig. 14 the dispersions are around 0.02 dex in dwarfs and 0.03 dex in giants for most el-

Fig. 11. Results for calcium. Left panel shows non-LTE results, right panel shows LTE results. Binned data for dwarfs ($\log g > 3.5$) and for giants ($\log g < 3.5$) are overplotted.
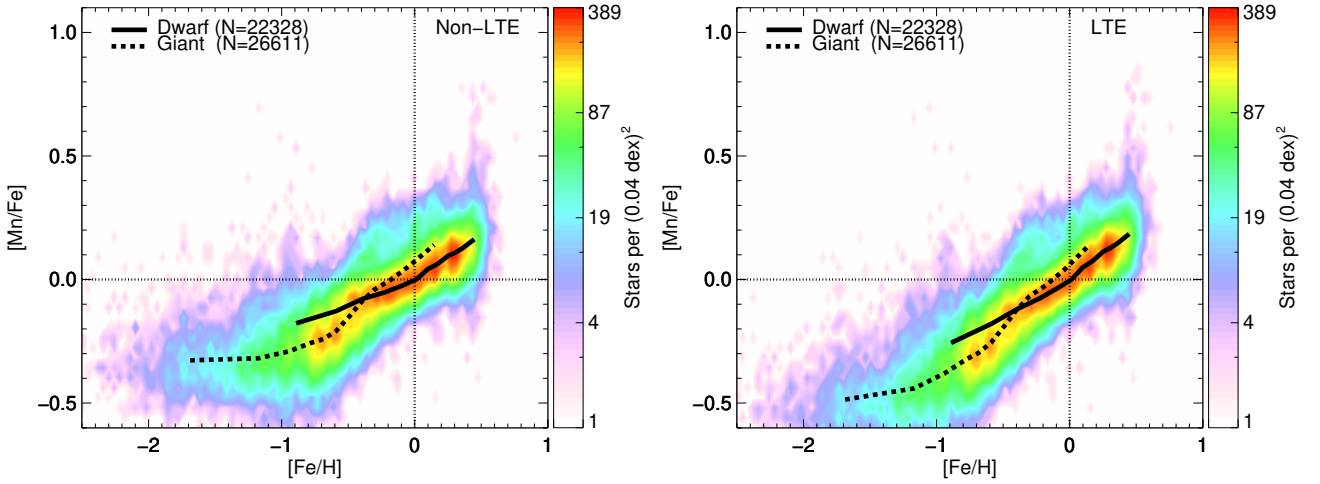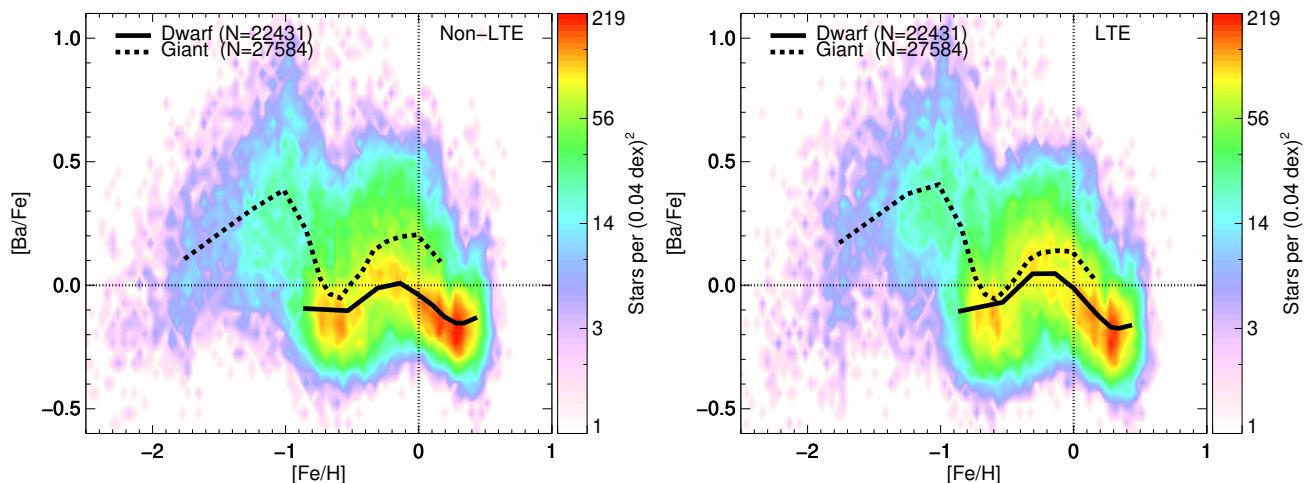

Fig. 12. Results for manganese. Left panel shows non-LTE results, right panel shows LTE results. Binned data for dwarfs ($\log g > 3.5$) and for giants ($\log g < 3.5$) are overplotted.

ements, in both LTE and non-LTE; they are slightly larger for lithium, carbon, and oxygen, namely around 0.03 dex in dwarfs, and 0.06 dex in giants. It is important to note that the dispersions in the results from multiple observations are much less than the star-to-star dispersions in the abundance results; if they were not, it would not be possible to see the impact of the assumption of LTE in the abundance plots of Sect. 3.3.

The assumption of LTE has a small impact on the line-to-line dispersions. This reflects both the random noise, as well as systematic errors arising from the pipeline, arising from deficiencies in modelling the stellar spectra, the impact of blends, and consistent offsets in the continuum placement. However, it may not reflect the entirety of the systematic errors, because the spectral lines being used for a particular element tend to have similar wavelengths and excitation potentials (Table 2), and thus tend to have similar sensitivities to systematic errors in the stellar parameters, and to neglected 3D or non-LTE effects. In Fig. 14 the dispersions are, in non-LTE, around 0.05 dex for dwarfs, and around 0.07 dex for giants. In LTE, they are typically only about

0.01 dex larger, owing to the cancellation effects obtained by using line-by-line solar abundances (Sect. 3.2).

Finally, the assumption of LTE does significantly impact the star-to-star dispersions. This reflects random noise and systematic errors in the pipeline, as well as intrinsic dispersion arising from different stars with the same [Fe/H] actually having different values of [A/Fe] in their atmospheres. The systematic errors are better represented here than in the line-to-line dispersions. In Fig. 14, in non-LTE and for most elements, the dispersions are around 0.05 to 0.15 dex for dwarfs and around 0.1 to 0.2 dex for giants, much larger than the dispersions in the results from multiple observations and also typically larger than the line-to-line dispersions. In LTE the star-to-star dispersions can be much larger: the largest difference is for magnesium and silicon in giants, where the dispersion is increased by around 0.10 dex.

It is difficult to make general conclusions about whether or not the non-LTE results shown in Figs 3 to 13 are dominated by intrinsic dispersion, or are dominated by systematics errors. The small dispersions in the results from multiple observations in Fig. 14 suggests that random noise are not dominating the

Fig. 13. Results for barium. Left panel shows non-LTE results, right panel shows LTE results. Binned data for dwarfs (log g > 3.5) and for giants (log g < 3.5) are overplotted.
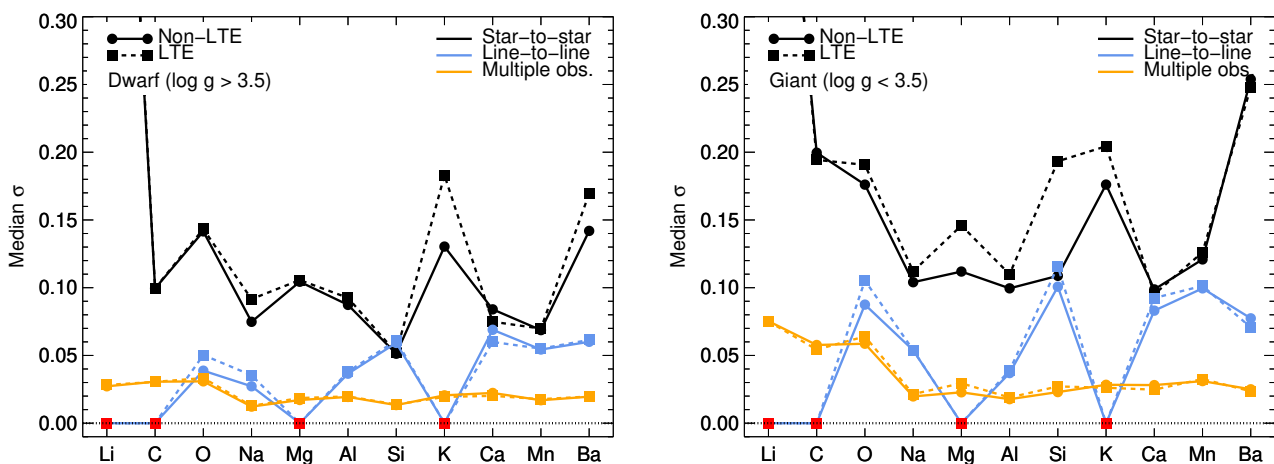
Fig. 14. Dispersions in the measured abundance results, in non-LTE and in LTE. 'Multiple obs.' (orange) show median standard deviations in [A/Fe] over multiple observations of the same stars. 'Line-to-line' (blue) show the median standard deviations in [A/Fe] over multiple spectral lines for the same star; lithium, carbon, magnesium, and potassium in red are set to zero because they were inferred from single lines. 'Star-to-star' (black) show the median standard deviation in [A/Fe] (or in log ϵ_A, in the case of lithium) across the different bins shown in Figs 3 to 13. Left panel shows results for dwarfs (log g > 3.5), right panel shows results for giants (log g < 3.5).

dispersions in the measured abundance relations. For lithium (Fig. 3), intrinsic dispersion is clearly dominant; lithium is fragile and easily destroyed in stellar atmospheres. Some elements such as calcium (Fig. 11) and silicon (Fig. 9) show tight abundance relations in non-LTE, and their star-to-star dispersions are similar to their line-to-line dispersions in Fig. 14, which suggests that systematics could be the limiting factor here. For other elements with broader measured abundance relations including aluminium (Fig. 8) and barium (Fig. 13), intrinsic effects could be dominant, although residual systematic errors still cannot be ruled out as discussed above.

5. Galactic chemical evolution and comparison with previous studies

In this section we briefly discuss the non-LTE abundance trends (Figs 3—13), and contrast them with results recently presented

elsewhere in the literature. The impact of the non-LTE effects were discussed in Sect. 4, and as such are not discussed again here.

5.1. Lithium

Lithium is a fragile element which was formed in the Big Bang (Fields 2011), and later in the cosmos from various sources but perhaps mainly from nova (Grisoni et al. 2019). The lithium abundances here confirm those recently presented in the literature. Fig. 3 shows a large intrinsic spread of abundances, with the dwarfs and giants following two distinct trends. Giant stars have covection zones that extend deeper into the stellar interior, to higher temperatures, and so lithium is gradually destroyed in these atmospheres. The most metal-poor dwarfs in the sample converge to around log $\epsilon_{Li} \approx 2.3$, the well-known 'Spite-plateau' (Spite & Spite 1982), and a mild increase in log ϵ_{Li} with increas-

ing [Fe/H] indicative of a gradual enrichment of lithium in the Galaxy as found in earlier studies of dwarf stars (Bensby & Lind 2018).

Also apparent is a significant drop in $\log \epsilon_{Li}$ at super-solar metallicities, as reported recently (Delgado Mena et al. 2015; Stonkutė et al. 2020). This may be a signature of radial migration (Guiglion et al. 2019). According to this picture, towards higher metallicities the stars in the sample are increasingly dominated by older stars that were born closer to the Galactic centre; given their age they have had time to both migrate outward to the solar neighbourhood, and to deplete significant amounts of their birth lithium abundance.

5.2. Carbon and oxygen

Carbon is a light element that is of interest as a tracer of AGB stars and of massive rotating stars (Karakas & Lattanzio 2014; Romano et al. 2019). The carbon abundances were determined from the high-excitation C I 658.8 nm line. This is usually too weak to be observed in cool giant stars: the steep trend seen in Fig. 4, based on a relatively small number of giant stars, may be due to the GALAH analysis pipeline interpreting noise as a detected line and should therefore be treated with skepticism. The Galactic evolution of carbon inferred here is thus based on the warmer dwarf stars. In the dwarfs, Fig. 4 shows a mild linear decrease in [C/Fe] from around 0.2 dex at [Fe/H] ≈ -0.5, to -0.1 dex at [Fe/H] $\approx +0.5$. This reflects that the cosmic production of iron from Type Ia supernova outpaces that of carbon from AGB stars or from massive stars.

Oxygen is an α-element that forms almost entirely via hydrostatic burning in massive stars (Kobayashi et al. 2006). The dwarfs and giants form parallel tracks in [O/Fe] versus [Fe/H] in Fig. 5, albeit offset by around 0.05 to 0.10 dex. This offset may reflect selection effects, the giants probing more of the α-rich Galactic thick disk (Sect. 4.3). There is a steep linear decrease in [O/Fe] from 0.5 dex at [Fe/H] ≈ -1.0, down to below -0.2 dex at [Fe/H] ≈ 0.5, that reflects that the cosmic production of iron from Type Ia supernova vastly outweighs that of oxygen from massive stars at high metallicities.

In general at moderate metallicities these results for carbon and oxygen are consistent with those from previous high-resolution, high signal-to-noise ratio studies (Bensby et al. 2014; Zhao et al. 2016; Amarsi et al. 2019b; Stonkutė et al. 2020). However they are not quite consistent with results for giants from APOGEE; these tend to find much flatter relationships, with a plateau in [O/Fe] or even a slight increase in [C/Fe] at super-solar metallicities (Hayes et al. 2018). The APOGEE abundances are inferred from molecular lines, prone to different systematics (in particular from 3D effects; Collet et al. 2007), and this may be the reason for the discrepancies.

In the metal-poor regime, [O/Fe] still shows a linear decrease with increasing [Fe/H], albeit with a more gentle slope, as well as a hint of a plateau at [Fe/H] ≈ -1.0, This is difficult to reconcile with the canonical picture of a α-abundance plateau at low metallicities, however it is roughly consistent with what was found in some previous studies of the O I 777 nm triplet (Ramírez et al. 2012; Amarsi et al. 2019b). Nevertheless, similar to carbon, the metal-poor trend is driven by the giants and should also be treated with skepticism because the high-excitation triplet is very weak in this regime. One or two of the weaker components becoming immeasurable over the noise, and perhaps spuriously measured, may also explain the relatively large star-to-star and line-to-line dispersions seen for oxygen in the giant stars in Fig. 14.

5.3. Sodium, aluminium, and potassium

Sodium, aluminium, and potassium are light elements with odd proton numbers, and with complicated cosmic origins. In Fig. 6 [Na/Fe] shows a plateau of around -0.1 dex at [Fe/H] $\lesssim -1.0$, followed by a jump of around 0.2 dex. Between $-1.0 \lesssim$ [Fe/H] $\lesssim$ 0.0, sodium abundances show a gentle decrease from 0.1 dex down to 0.0 dex. At super-solar metallicities, [Na/Fe] increases again, reaching 0.25 dex at [Fe/H] ≈ 0.5.

Aluminium and potassium appear quite similar to the α-elements (Sect. 5.4), at least below [Fe/H] $\lesssim 0.0$. In Fig. 8 there appears an aluminium-poor component with [Al/Fe] ≈ 0.0, and and an aluminium-rich component with [Al/Fe] ≈ 0.25 (traced by dwarfs and giants respectively; Sect. 4.3). Similarly, in Fig. 10 [K/Fe] shows a plateau at around 0.25 dex below [Fe/H] $\lesssim -1.0$, and a mild decrease down to [Fe/H] ≈ 0.0.

At super-solar metallicities, however, aluminium behaves qualitatively similar to sodium. In the dwarfs, [Al/Fe] increasing from 0.0 dex at [Fe/H] ≈ 0.0, to 0.2 dex at [Fe/H] ≈ 0.5. In contrast, potassium shows a flat trend, similar to the canonical α-elements magnesium, silicon, and calcium (Sect. 5.4).

The sodium, aluminium, and potassium abundances thus show a varied behaviour that is indicative of multiple different cosmic origins and enrichment on different timescales. These results are difficult to explain comprehensively with models of Galactic chemical evolution (Smiljanic et al. 2016; Reggiani et al. 2019). Nevertheless, the sodium abundances are qualitatively consistent with what has been found in other recent high-resolution, high signal-to-noise ratio studies (Bensby et al. 2014; Zhao et al. 2016), while the aluminium and potassium abundances agree well with results for giants from APOGEE (Hayes et al. 2018).

However, as pointed out already in Sect. 4.3, there is an offset between the dwarfs and giants for aluminium of around 0.2 dex. Since the trends have similar shapes despite the offset, they would be calibrated away in the APOGEE results, which are strictly for giants. Interestingly, Gaia-ESO find a similar offset between dwarfs and giants (Smiljanic et al. 2016), albeit to a smaller extent. In the present study, we suspect that the offset signals residual systematic errors in the aluminium abundances.

5.4. Magnesium, silicon, and calcium

These canonical α-elements have been discussed copiously in the literature, and the results presented here should not prove controversial. The results for magnesium, silicon, and calcium each display the usual dichotomy (McWilliam 1997) between the α-poor thin disk and the α-rich thick disk (traced by dwarfs and giants respectively; Sect. 4.3). In Figs 7, 9, and 11, this thick disk forms a plateau at around [A/Fe] ≈ 0.25 below [Fe/H] $\lesssim$ -1.0. These results are quantitatively consistent with recent high-resolution, high signal-to-noise ratio studies (Bensby et al. 2014; Zhao et al. 2016; Mashonkina et al. 2019). At super-solar metallicities these elements tend to show flat trends of around 0.0 dex, which is consistent with results for giants from APOGEE (Hayes et al. 2018).

5.5. Manganese

Manganese is an iron-peak element that forms primarily in Type Ia supernova, and is currently of considerable interest in constraining the progenitors and explosion properties of these events (Kobayashi et al. 2019; de los Reyes et al. 2020; Eitner et al. 2020) Fig. 12 shows [Mn/Fe] increases linearly from -0.3 dex

at [Fe/H] $\approx$ −1.0, to around 0.2 dex at [Fe/H] $\approx$ 0.5; at lower metallicities there is a plateau with [Mn/Fe] $\approx$ −0.3. These trends are quantitatively consistent with results for dwarfs (Mishenina et al. 2015), and for giants from APOGEE (Hayes et al. 2018).

5.6. Barium

Barium is a heavy element that is mainly produced via the slow neutron capture process at least at high metallicities (Skúladóttir et al. 2020), probably in AGB stars (Karakas & Lattanzio 2014). In Fig. 13 the majority of stars sit at around [Ba/Fe] $\approx$ −0.1 at [Fe/H] $\approx$ −1.0, gradually rise to [Ba/Fe] $\approx$ 0.25 at [Fe/H] $\approx$ −0.25, and decrease again to [Ba/Fe] $\approx$ 0.0 at [Fe/H] $\approx$ 0.25. At lower metallicities the barium abundances are slightly elevated, at around [Ba/Fe] $\approx$ 0.5 at [Fe/H] $\lesssim$ −1.0. There is a large dispersion in Fig. 13, with the results for the giants being skewed to higher barium abundances,

The general behaviour of a peak at slightly sub-solar metallicities is in fact qualitatively similar to what was found in the recent study of Delgado Mena et al. (2017), and in the non-LTE study of Korotin et al. (2011). In contrast however, other studies tend to find a flat trend in [Ba/Fe], or one that very gradually increases with increasing [Fe/H] (Mishenina et al. 2013; Bensby et al. 2014). The actual nature of the [Ba/Fe] versus [Fe/H] trend thus appears to be relatively poorly constrained.

6. Conclusion

We have presented extensive grids of departure coefficients for 13 different elements, calculated on standard MARCS model atmospheres. These data are publicly available via Zenodo (link here), or by contacting the lead author directly. They will also be distributed with SME and PySME (link here). The departure coefficients can be implemented into existing stellar analyses pipelines, to simply and cheaply account for departures from LTE for a large number of spectral lines.

We illustrated this latter point by implementing the grids into the GALAH analysis pipeline, that is based on the 1D spectrum synthesis code SME. The grids of departure coefficients clearly make an impact on large stellar surveys. The grids lead to differences in the mean [A/Fe] at given [Fe/H] of as much as 0.2 dex. This resulting in qualitatively different pictures of the Galactic chemical evolution, for example giving rise to metal-poor plateaus in [Mg/Fe] (Fig. 7), [K/Fe] (Fig. 10), and [Mn/Fe] (Fig. 12), whereas a steep increase with increasing [Fe/H] would be seen in LTE. The grids affect different parts of stellar parameter space differently, and thus for example remove offsets in [Na/Fe] of up to around 0.2 dex between dwarfs and giants (Fig. 6). The grids generally reduce the dispersion in the [A/Fe] versus [Fe/H] plane (Fig. 14), by as much as 0.10 dex in the case of [Si/Fe] (Fig. 9).

Future efforts will extend these calculations to more elements in the periodic table. This will make it possible to model even more elements in non-LTE, in GALAH as well as in other large spectroscopic surveys. This is a necessary step towards getting elemental abundances that are accurate to the 0.05 dex level, for of the order millions of stars.

We caution that there are nevertheless other systematics in stellar models that still would need to be addressed. After taking departures from LTE into account, the next step may be to consider the effects of stellar convection (Nissen & Gustafsson 2018). Unfortunately 3D non-LTE corrections (Amarsi et al.

2019b) cannot be implemented into existing stellar analyses pipelines in an analogous way to these precomputed grids of 1D non-LTE departure coefficients; at present, grids of line-by-line 3D non-LTE abundance corrections are still required. However, in the more distant future, stellar analyses pipelines may move towards using 3D spectrum synthesis codes, and to using precomputed grids of 3D non-LTE departure coefficients.

It is also unclear to what extent departures from LTE may impact the atmospheric stratifications themselves (Short & Hauschildt 2005). The grids of departure coefficients presented here offer a way forward towards relaxing the LTE assumption in the construction of 1D model atmospheres. The departure coefficients for the key electron donors could be fed back into the model atmosphere code for a final iteration, to see the impact of departures from LTE on the atmospheric temperature stratification. This will be investigated in a future study.

References

Ahumada, R., Allende Prieto, C., Almeida, A., et al. 2019, arXiv e-prints, arXiv:1912.02905
Allende Prieto, C., Asplund, M., & Fabiani Bendicho, P. 2004, A&A, 423, 1109
Amarsi, A. M. & Asplund, M. 2017, MNRAS, 464, 264
Amarsi, A. M., Asplund, M., Collet, R., & Leenaarts, J. 2016a, MNRAS, 455, 3735
Amarsi, A. M., Barklem, P. S., Asplund, M., Collet, R., & Zatsarinny, O. 2018a, A&A, 616, A89
Amarsi, A. M., Barklem, P. S., Collet, R., Grevesse, N., & Asplund, M. 2019a, A&A, 624, A111
Amarsi, A. M., Grevesse, N., Grumer, J., et al. 2020, A&A, 636, A120
Amarsi, A. M., Lind, K., Asplund, M., Barklem, P. S., & Collet, R. 2016b, MNRAS, 463, 1518
Amarsi, A. M., Nissen, P. E., & Skúladóttir, Á. 2019b, A&A, 630, A104
Amarsi, A. M., Nordlander, T., Barklem, P. S., et al. 2018b, A&A, 615, A139
Asplund, M. 2005, ARA&A, 43, 481
Asplund, M., Grevesse, N., & Sauval, A. J. 2005, in Astronomical Society of the Pacific Conference Series, Vol. 336, Cosmic Abundances as Records of Stellar Evolution and Nucleosynthesis, ed. T. G. Barnes, III & F. N. Bash, 25
Asplund, M., Grevesse, N., Sauval, A. J., & Scott, P. 2009, ARA&A, 47, 481
Barklem, P. S. 2016a, A&A Rev., 24, 9
Barklem, P. S. 2016b, Phys. Rev. A, 93, 042705
Barklem, P. S., Belyaev, A. K., & Asplund, M. 2003, A&A, 409, L1
Barklem, P. S., Belyaev, A. K., Dickinson, A. S., & Gadéa, F. X. 2010, A&A, 519, A20
Barklem, P. S., Belyaev, A. K., Guitou, M., et al. 2011, A&A, 530, A94
Barklem, P. S., Belyaev, A. K., Spielfiedel, A., Guitou, M., & Feautrier, N. 2012, A&A, 541, A80
Barklem, P. S. & Collet, R. 2016, A&A, 588, A96
Bedell, M., Bean, J. L., Meléndez, J., et al. 2018, ApJ, 865, 68
Belyaev, A. K. 2013, Phys. Rev. A, 88, 052704
Belyaev, A. K. & Barklem, P. S. 2003, Phys. Rev. A, 68, 062703
Belyaev, A. K., Barklem, P. S., Dickinson, A. S., & Gadéa, F. X. 2010, Phys. Rev. A, 81, 032706
Belyaev, A. K., Barklem, P. S., Spielfiedel, A., et al. 2012, Phys. Rev. A, 85, 032704
Belyaev, A. K. & Yakovleva, S. A. 2017, A&A, 606, A147
Bensby, T., Feltzing, S., & Oey, M. S. 2014, A&A, 562, A71
Bensby, T. & Lind, K. 2018, A&A, 615, A151
Bergemann, M., Gallagher, A. J., Eitner, P., et al. 2019, A&A, 631, A80

Bergemann, M., Hansen, C. J., Bautista, M., & Ruchti, G. 2012, A&A, 546, A90
Buder, S., Asplund, M., Duong, L., et al. 2018, MNRAS, 478, 4513
Chang, T. N. & Tang, X. 1990, J. Quant. Spectr. Rad. Transf., 43, 207
Collet, R., Asplund, M., & Trampedach, R. 2007, A&A, 469, 687
Dalton, G., Trager, S., Abrams, D. C., et al. 2016, in Proc. SPIE, Vol. 9908, Ground-based and Airborne Instrumentation for Astronomy VI, 99081G
Davidson, M. D., Snoek, L. C., Volten, H., & Doenszelmann, A. 1992, A&A, 255, 457
de Jong, R. S., Agertz, O., Berbel, A. A., et al. 2019, The Messenger, 175, 3
de los Reyes, M. A. C., Kirby, E. N., Seitenzahl, I. R., & Shen, K. J. 2020, ApJ, 891, 85
De Silva, G. M., Freeman, K. C., Bland-Hawthorn, J., et al. 2015, MNRAS, 449, 2604
Delgado Mena, E., Bertrán de Lis, S., Adibekyan, V. Z., et al. 2015, A&A, 576, A69
Delgado Mena, E., Tsantaki, M., Adibekyan, V. Z., et al. 2017, A&A, 606, A94
Den Hartog, E. A., Lawler, J. E., Sobeck, J. S., Sneden, C., & Cowan, J. J. 2011, ApJS, 194, 35
Drawin, H.-W. 1968, Z. Phys., 211, 404
Drawin, H. W. 1969, Z. Phys., 225, 483
Eitner, P., Bergemann, M., Hansen, C. J., et al. 2020, A&A, 635, A38
Feuillet, D. K., Frankel, N., Lind, K., et al. 2019, MNRAS, 489, 1742
Fields, B. D. 2011, Annual Review of Nuclear and Particle Science, 61, 47
Froese Fischer, C., Tachiev, G., & Irimia, A. 2006, At. Data Nucl. Data Tables, 92, 607
Gaia Collaboration, Brown, A. G. A., Vallenari, A., et al. 2018, A&A, 616, A1
Gallagher, A. J., Bergemann, M., Collet, R., et al. 2020, A&A, 634, A55
García Pérez, A. E., Allende Prieto, C., Holtzman, J. A., et al. 2016, AJ, 151, 144
Garz, T. 1973, A&A, 26, 471
Grevesse, N., Asplund, M., & Sauval, A. J. 2007, The Solar Chemical Composition, ed. R. von Steiger, G. Gloeckler, & G. M. Mason (Springer Science+Business Media), 105
Grisoni, V., Matteucci, F., Romano, D., & Fu, X. 2019, MNRAS, 489, 3539
Guiglion, G., Chiappini, C., Romano, D., et al. 2019, A&A, 623, A99
Gustafsson, B., Edvardsson, B., Eriksson, K., et al. 2008, A&A, 486, 951
Hayden, M. R., Bovy, J., Holtzman, J. A., et al. 2015, ApJ, 808, 132
Hayes, C. R., Majewski, S. R., Shetrone, M., et al. 2018, ApJ, 852, 49
Hibbert, A., Biemont, E., Godefroid, M., & Vaeck, N. 1991, J. Phys. B, 24, 3943
Hibbert, A., Biemont, E., Godefroid, M., & Vaeck, N. 1993, A&AS, 99, 179
Hubeny, I. & Mihalas, D. 2014, Theory of Stellar Atmospheres (Princeton Univ. Press, Princeton, NJ)
Ibgui, L., Hubeny, I., Lanz, T., & Stehlé, C. 2013, A&A, 549, A126
Kao, C.-Y. J. & Auer, L. H. 1990, Monthly Weather Review, 118, 1551
Karakas, A. I. & Lattanzio, J. C. 2014, PASA, 31, e030
Karovicova, I., White, T. R., Nordlander, T., et al. 2018, MNRAS, 475, L81
Kaulakys, B. P. 1985, J. Phys. B, 18, L167
Kaulakys, B. P. 1986, JETP, 91, 391
Kaulakys, B. P. 1991, J. Phys. B, 24, L127
Kelleher, D. E. & Podobedova, L. I. 2008, J. Phys. Chem. Ref. Data, 37, 709
Kobayashi, C., Leung, S.-C., & Nomoto, K. 2019, arXiv e-prints, arXiv:1906.09980
Kobayashi, C., Umeda, H., Nomoto, K., Tominaga, N., & Ohkubo, T. 2006, ApJ, 653, 1145
Korotin, S., Mishenina, T., Gorbaneva, T., & Soubiran, C. 2011, MNRAS, 415, 2093
Korotin, S. A., Andrievsky, S. M., Hansen, C. J., et al. 2015, A&A, 581, A70
Kos, J., Lin, J., Zwitter, T., et al. 2017, MNRAS, 464, 1259
Lambert, D. L. 1993, Physica Scripta Volume T, 47, 186
Leenaarts, J. & Carlsson, M. 2009, in Astronomical Society of the Pacific Conference Series, Vol. 415, The Second Hinode Science Meeting, ed. B. Lites, M. Cheung, T. Magara, J. Mariska, & K. Reeves, 87
Lind, K., Amarsi, A. M., Asplund, M., et al. 2017, MNRAS, 468, 4311
Lind, K., Asplund, M., Barklem, P. S., & Belyaev, A. K. 2011, A&A, 528, A103
Lind, K., Bergemann, M., & Asplund, M. 2012, MNRAS, 427, 50
Lind, K., Melendez, J., Asplund, M., Collet, R., & Magic, Z. 2013, A&A, 554, A96
Mashonkina, L. I., Neretina, M. D., Sitnova, T. M., & Pakhomov, Y. V. 2019, Astronomy Reports, 63, 726
Mashonkina, L. I., Sitnova, T. N., & Pakhomov, Y. V. 2016, Astronomy Letters, 42, 606
McWilliam, A. 1997, ARA&A, 35, 503
Mihalas, D. & Athay, R. G. 1973, ARA&A, 11, 187
Mishenina, T., Gorbaneva, T., Pignatari, M., Thielemann, F. K., & Korotin, S. A. 2015, MNRAS, 454, 1585
Mishenina, T. V., Pignatari, M., Korotin, S. A., et al. 2013, A&A, 552, A128
Ness, M., Hogg, D. W., Rix, H.-W., Ho, A. Y. Q., & Zasowski, G. 2015, ApJ, 808, 16
Nissen, P. E. 2015, A&A, 579, A52
Nissen, P. E. & Gustafsson, B. 2018, A&A Rev., 26, 6

Nordlander, T. & Lind, K. 2017, A&A, 607, A75
O'Brian, T. R. & Lawler, J. E. 1991, Phys. Rev. A, 44, 7134
Osorio, Y., Allende Prieto, C., Hubeny, I., Mészáros, S., & Shetrone, M. 2020, A&A, 637, A80
Osorio, Y. & Barklem, P. S. 2016, A&A, 586, A120
Osorio, Y., Barklem, P. S., Lind, K., et al. 2015, A&A, 579, A53
Osorio, Y., Lind, K., Barklem, P. S., Allende Prieto, C., & Zatsarinny, O. 2019, A&A, 623, A103
Piskunov, N. & Valenti, J. A. 2017, A&A, 597, A16
Ramírez, I., Meléndez, J., & Chanamé, J. 2012, ApJ, 757, 164
Randich, S., Gilmore, G., & Gaia-ESO Consortium. 2013, The Messenger, 154, 47
Recio-Blanco, A., de Laverny, P., Allende Prieto, C., et al. 2016, A&A, 585, A93
Reggiani, H., Amarsi, A. M., Lind, K., et al. 2019, A&A, 627, A177
Romano, D., Matteucci, F., Zhang, Z.-Y., Ivison, R. J., & Ventura, P. 2019, MNRAS, 490, 2838
Rutten, R. J. 2003, Radiative Transfer in Stellar Atmospheres, 8th edn. (Utrecht University)
Rybicki, G. B. & Hummer, D. G. 1992, A&A, 262, 209
Saad, Y. 2003, Iterative methods for sparse linear systems, Vol. 82 (siam)
Short, C. I. & Hauschildt, P. H. 2005, ApJ, 618, 926
Silva Aguirre, V., Casagrande, L., Basu, S., et al. 2012, ApJ, 757, 99
Skúladóttir, Á., Hansen, C. J., Choplin, A., et al. 2020, A&A, 634, A84
Smiljanic, R., Romano, D., Bragaglia, A., et al. 2016, A&A, 589, A115
Smith, G. 1988, J. Phys. B, 21, 2827
Smith, G. & Raggett, D. S. J. 1981, J. Phys. B, 14, 4015
Spina, L., Meléndez, J., & Ramírez, I. 2016, A&A, 585, A152
Spite, F. & Spite, M. 1982, A&A, 115, 357
Steenbock, W. & Holweger, H. 1984, A&A, 130, 319
Steinmetz, M., Guiglion, G., McMillan, P. J., et al. 2020, arXiv e-prints, arXiv:2002.04512
Stonkutė, E., Chorniy, Y., Tautvaišienė, G., et al. 2020, AJ, 159, 90
Thomson, J. J. 1912, The London, Edinburgh, and Dublin Philosophical Magazine and Journal of Science, 23, 449
Ting, Y.-S., Conroy, C., Rix, H.-W., & Cargile, P. 2019, ApJ, 879, 69
Trubko, R., Gregoire, M. D., Holmgren, W. F., & Cronin, A. D. 2017, Phys. Rev. A, 95, 052507
Valenti, J. A. & Piskunov, N. 1996, A&AS, 118, 595
Xiang, M., Ting, Y.-S., Rix, H.-W., et al. 2019, ApJS, 245, 34
Yan, Z.-C., Tambasco, M., & Drake, G. W. F. 1998, Phys. Rev. A, 57, 1652
Zhao, G., Mashonkina, L., Yan, H. L., et al. 2016, ApJ, 833, 225
Zhao, G., Zhao, Y.-H., Chu, Y.-Q., Jing, Y.-P., & Deng, L.-C. 2012, Res. Astron. Astrophys., 12, 723